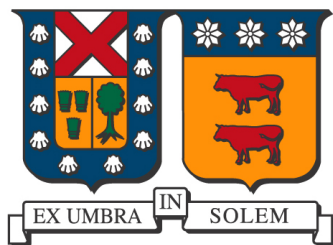


DEPARTAMENTO DE FÍSICA  
UNIVERSIDAD TÉCNICA FEDERICO SANTA MARIA



PhD Thesis

# Modern detectors to study the Standard Model and beyond

Author:  
Gerardo Vásquez Arenas

Supervisor:  
Professor Sergey Kuleshov

Valparaíso, 2017



---

# Abstract

The increased necessity of experimental proof of physics beyond Standard Model (SM) and Dark Matter theories leads us to develop new detectors for high energy experiments, such as ATLAS with its upgrade (New Small Wheel project in particular) for the luminosity increase at LHC, and a new experiment on SPS facilities at CERN called NA64 to search for Dark Matter on invisible (visible) decays of dark photons.

For these two experiments, detectors from the Physics department of the Technical University Federico Santa Maria in Valparaiso (Chile) have been built **to be part of such enterprise.**

Characterizations and tests have been conducted with the use of particles beam (electrons, pions, muons and gamma rays) from the Experimental Area at CERN.



---

# Dedication



---

## Acknowledgments



---

# Agradecimientos



# Contents

<b>1. Introduction</b>	<b>13</b>
1.1. Interaccion of Radiation with Matter . . . . .	13
1.2. Gas fillld detectors . . . . .	13
1.2.1. Production of Electron-Ion pairs . . . . .	13
1.2.2. Diffusion and Drift of Charges in Gases . . . . .	13
1.2.3. Regions of Operation of Gas Filled Detectors . . . . .	13
1.3. Scintillation detectors . . . . .	13
1.4. Calorimeters . . . . .	13
1.4.1. Radiation Length . . . . .	13
<b>2. Small-strip Thin Gap Chamber</b>	<b>15</b>
2.1. High Luminosity Large Hadron Collider . . . . .	15
2.2. ATLAS Detector . . . . .	17
2.2.1. Coordinate system . . . . .	18
2.2.2. Detector Upgrade . . . . .	19
2.3. sTGC Description . . . . .	20
2.3.1. Electric field simulation . . . . .	21
2.4. Construction process . . . . .	22
2.5. Gain uniformity measurements . . . . .	26
2.5.1. Setup . . . . .	26
2.5.2. Results . . . . .	28
2.6. Stability under high rate . . . . .	30
2.7. Spatial Resolution . . . . .	35
2.7.1. Analysis Model . . . . .	36
2.8. Pad efficiency . . . . .	41
2.9. Summary . . . . .	43
<b>3. High count rate <math>\gamma</math>-ray spectroscopy in GIF++</b>	<b>45</b>
<b>4. Synchrotron radiation detector for <math>e^-</math> tagging</b>	<b>47</b>
<b>5. Conclusion</b>	<b>49</b>

<b>A. Appendix</b>	<b>51</b>
A.1. Mechanical Measurements sTGC Module 0 . . . . .	51
A.2. PMT RT7525 Data Sheet . . . . .	51
A.3. NA64 Experiment:Data structure . . . . .	51
A.4. NA64 Experiemnt:DAQ system . . . . .	51

---

# 1. Introduction

In this chapter we present a review of the physics for radiation detectors. The basic features of radiation detectors can be understood once fundamental processes of radiation interaction in matter are considered.

## 1.1. Interaction of Radiation with Matter

5 pages

## 1.2. Gas filled detectors

5 pages

### 1.2.1. Production of Electron-Ion pairs

### 1.2.2. Diffusion and Drift of Charges in Gases

### 1.2.3. Regions of Operation of Gas Filled Detectors

## 1.3. Scintillation detectors

3 pages

## 1.4. Calorimeters

### 1.4.1. Radiation Length

The radiation length is the distance over which the radiative emission is the dominant energy loss process and the screening parameter  $\eta$  approaches to 0, the total radiation cross section is that for complete screening except in the case of high frequency emitted photons. This cross section does not depend on the incoming electron energy  $E_0$ . For a complete screening in the Born approximation, the quantity  $X_0$  is introduced as:

$$X_0 = \frac{1}{[4n_A \bar{\Phi}_c \ln \left( \frac{183}{Z^{1/3}} \right)]} \text{[cm]} \quad (1.1)$$

4 pages

---

## 2. Small-strip Thin Gap Chamber

The aim of this chapter is to show the characteristics of new detectors to be used as part of the ATLAS experiment upgrade, and how to achieve the requirements of the high luminosity operation. The results of each test to characterize the detector are presented in this chapter.

### 2.1. High Luminosity Large Hadron Collider

The Large Hadron Collider (LHC), located at the European Organization for Nuclear Research (CERN, derived from *Conseil Européen pour la Recherche Nucléaire*) at the Franco-Swiss border near Geneva is a circular accelerator of 27km circumference of acceleration pipes, constitutes the largest scientific instrument ever designed and built for scientific research. It has been successfully commissioned in March 2010 for proton-proton collision with a 7 GeV center-of-mass energy.

The LHC is pushing the limits of human knowledge, enabling physicists to go beyond the Standard Model (SM): the enigmatic Higgs boson, the mysterious Dark Matter and the world of super symmetry are just three of the long-awaited mysteries that the LHC is working to unveil.

The announcement given by CERN on 4 July 2012 about the discovery of a new boson at 125-126GeV[1, 2], almost certainly the long awaited Higgs particle, is the first fundamental discovery, hopefully the first of a series, that the LHC can deliver. Such discovery was made possible thanks to the general-purpose detectors ATLAS and CMS, both located at 2 interaction regions, complemented by the specialized detectors ALICE and LHCb.

	Period	Energy $\sqrt{s}$	Luminosity $\mathcal{L}$	Integrate $\mathcal{L}$
Run I	2010-2012	7-8 TeV	$6 \times 10^{33} \text{ cm}^{-2}\text{s}^{-1}$	$25 \text{ fb}^{-1}$
LS1	2013-2014	LHC: Go to design energy, nominal luminosity, bunch spacing 25ns		
Phase 0	2015-2018	14 TeV	$1 \times 10^{34} \text{ cm}^{-2}\text{s}^{-1}$	$75 \text{ fb}^{-1}$ to $100 \text{ fb}^{-1}$
LS2	2019-2020	ATLAS: Upgrade $\mu$ spectrometer;NSW,LAr Calorimeter & FTK		
Phase 1	2021-2023	14 TeV	$2 \times 10^{34} \text{ cm}^{-2}\text{s}^{-1}$	$\sim 350 \text{ fb}^{-1}$
LS3	2024-2025	ATLAS: New Inner Tracker and trigger architecture		
Phase 2	2026-2030	14 TeV	$5 \times 10^{34} \text{ cm}^{-2}\text{s}^{-1}$	$\sim 3000 \text{ fb}^{-1}$

Table 2.1: LHC Schedule & upgrades for ATLAS detector.

The LHC baseline programme until 2030 is shown in Table 2.1. After entering into the nominal energy regime of 13 TeV to 14 TeV centro-fo-mass energy in 2015, it is expected that the LHC will reach the design luminosity of  $1 \times 10^{34} \text{ cm}^{-2}\text{s}^{-2}$ . This peak value should give a total integrated luminosity of about  $40 \text{ fb}^{-1}$  per year. In the period 2019-2023 the LHC will hopefully further increase to two times the peak luminosity, reaching at the end of 2023 an integrated luminosity of about  $350 \text{ fb}^{-1}$ .

After the Long Shutdown 3 (LS3) the machine will be in the High Luminosity configuration (HL-LHC). For its successful realization, a number of key novel technologies have to be developed, validated, and integrated, accompanied with upgrades from the general purpose detectors such as ATLAS.

## 2.2. ATLAS Detector

The ATLAS detector is a general-purpose experiment, designed to explore proton-proton collisions at center of mass up to  $\sqrt{s} = 14 \text{ GeV}$  in the Large Hadron Collider (LHC) at the European Laboratory for Particle Physics (CERN). It is aiming to understand the foundations of matter and forces, in particular the nature of mass in a broad physics program. The ATLAS detector was built with the ability to discover the Higgs boson over a wide mass range. It can also perform searches for the production of heavy particles that would indicate physics beyond the Standard Model, such as super symmetric particles, as well as searches for other massive objects.

The ATLAS experiment includes complex detector systems. The central part is a cylindrical Inner Detector, to detect charged particles produced in the collisions, and as such, it is a compact and highly sensitive component. It consists of three different systems of sensors, all immersed in a magnetic field parallel to the beam axis. The **Inner Detector** measures the direction, momentum, and charge of electrically-charged particles produced in each proton-proton collision. The next part is the Calorimeter (red and green on figure 2.1), which measures the energy of a particle when it loses its energy as it passes through the detector. It is usually designed to stop entirely or “absorb” most of the particles coming from a collision, forcing them to deposit all of their energy within the detector. Calorimeters typically consist of layers of “passive” or “absorbing” high-dense material -for example, lead-interleaved with layers of an “active” medium such as scintillator or liquid argon.

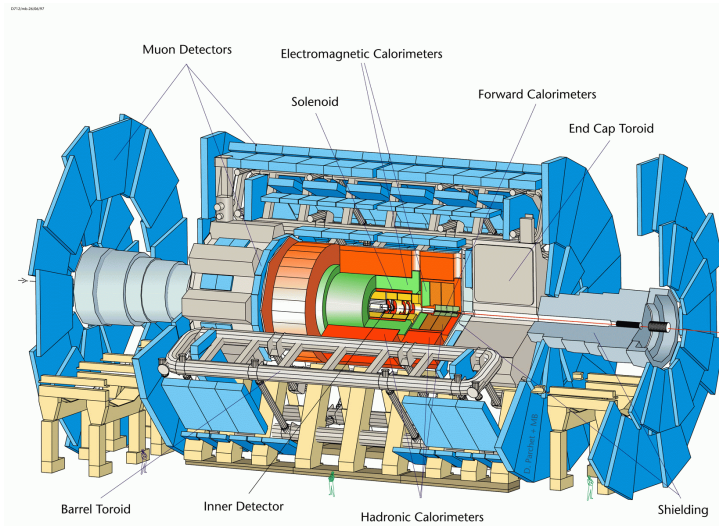


Figure 2.1: ATLAS detector, Muon Spectrometer (in blue)

Electromagnetic calorimeters measure the energy of electrons and photons as they interact with matter. Hadronic calorimeters sample the energy of hadrons (particles that contain quarks, such as protons and neutrons) as they interact with atomic nuclei. The components of the ATLAS calorimetry system are: the **Liquid Argon (LAr) Calorimeter** and the **Tile Hadronic Calorimeter**.

Calorimeters can stop most known particles except muons and neutrinos. Muons are charged particles that pass through the Inner Detector and Calorimeter interacting only by ionization, they can penetrate through large amount of material without any strong interaction, they have long lifetime, therefore, can be considered as stable particles within the detector's volume, and provide a good tagging for the lepton's decays channels.

To trigger and detect these particles, the ATLAS experiment uses the **Muon Spectrometer**, made up of 4.000 individual muon chambers (different types of gas chambers) which are in charge of identify each one of these muons. It is only possible to measure their momentum with the help of the **Magnet System**, made of three sections; the **Central Solenoid Magnet** with a 2T magnetic field that bends the charged particles for momentum measurement near the interaction points, helping the Inner Tracker system, the **Barrel Toroid** bends the muon particles in the low rapidity region, and the **Endcap Toroid** with a 4T magnetic field that bends the muons in the high rapidity region.

### 2.2.1. Coordinate system

A common coordinate system is used through ATLAS. The interaction point is defined as the origin of the coordinate system. The z-axis runs along the beam line. The x-y plane is perpendicular to the beam line and is referred to as the transverse momentum,  $p_T$ . The positive x-axis points from the interaction point to the center of the LHC ring; the positive y-axis points upward to the surface of the earth. The detector which is located half at positive z-values is referred to as the “A-side”, to the other half the “C-side”. The

transverse plane is often described in terms of  $r - \phi$  coordinates. The azimuthal angle  $\phi$  is measured from the x-axis, around the beam. The radial dimension,  $r$ , measures the distance from the beam line. The polar angle  $\theta$  is defined as the angle from the positive z-axis. The polar angle is often reported in terms of pseudorapidity, defined as  $\eta = -\ln \tan(\theta/2)$ . The distances  $\Delta R$  is defined in  $\eta - \phi$  space as  $\Delta R = \sqrt{\Delta\eta^2 + \Delta\phi^2}$ .

### 2.2.2. Detector Upgrade

To fulfill the LHC program (in table 2.1), and in order to benefit from the expected high luminosity performance that will be provided by the Phase-I upgraded LHC, the first station of ATLAS muon end-cap system (Small Wheel, SW) will need to be replaced. The **New Small Wheel (NSW)** will have to operate in a high background providing a radiation region (up to  $15\text{ kHz/cm}^2$  of photons, and  $75\text{ Hz/cm}^2$  of neutrons is expected) while reconstructing muon tracks with high precision as well as furnishing information for the Level-1 trigger. These performance criteria are demanding. In particular, the precision reconstruction of tracks for offline analysis requires a spatial resolution of about  $100\mu\text{m}$ , and the Level-1 trigger track segments have to be reconstructed online with an angular resolution of approximately 1mrad.

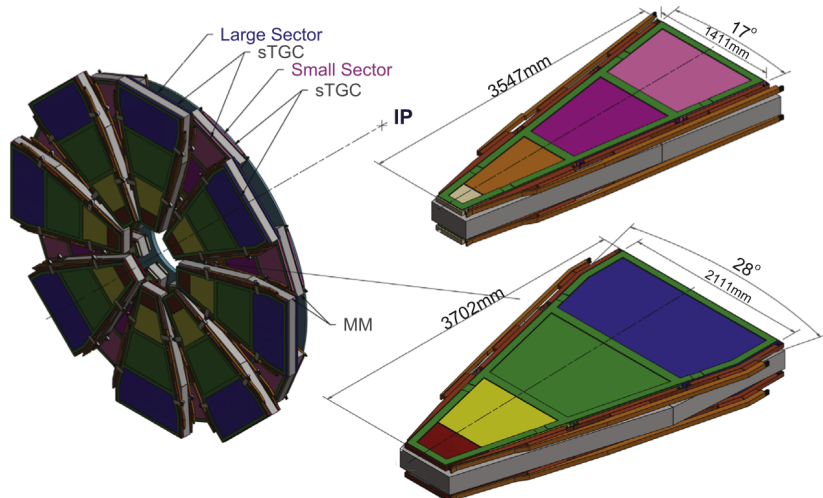


Figure 2.2: New Small Wheel

The NSW will have two chamber technologies, one primarily devoted to the Level-1 trigger function (Small-strip Thin Gap Chambers, sTGC) and the other one dedicated to precision tracking (Micromegas detectors, MM). The sTGC is deployed for triggering given their single bunch crossing identification capability, a fast response and good position resolution.

The MM detectors have exceptional precision tracking capabilities due to their small gap (5mm) and strip pitch (approximately 0.5mm). Such a precision is crucial to maintain the current ATLAS muon momentum resolution in the high background environment of

the upgraded LHC. The MM chambers can, at the same time, confirm the existence of track segments found by the muon end-cap middle station (Big Wheels) online. The sTGC has the additional ability to measure offline muon tracks with good precision, so the sTGC-MM chamber technology combination forms a fully redundant detector system for triggering and tracking both for online and offline functions. This detector combination has been designed to be able to provide excellent performance for the eventual High Luminosity LHC upgrade.

## 2.3. sTGC Description

The small-strip Thin Gap Chamber (a.k.a sTGC) is a multi-wire proportional chamber (MWPC), a detector type with a relatively old technology. Its successful introduction to detector systems in 1968 has earned eGeorges Charpak the Nobel prize in Physics 1992. Those devices have been a major ingredient to detector systems since they can achieve spatial resolution of tenths microns, and have typical time resolution of about 50ns.

The sTGC has been design to exploit these features, working with a cathode-anode pitch smaller than the anode-anode pitch, mostly based on the design of the Thin Gap Chamber[3], with thinner strips as the main improvement from the previous version. The TGC technology has been used since 1988 in the OPAL experiment[4] and is currently part of the muon spectrometer in ATLAS.

This new chamber has the advantage of having a 3.2mm strip-pitch compared with the 6mm from the previous TGC, which explains the *small-strip* prefix.

Chambers with different strips sizes were built and tested under pion beams, and the 3.2mm pitch was chosen as the best option to provide a resolution better than  $100\mu\text{m}$ [5]. This change will improve the measurement of charge centroid position by charge interpolation.

To improve the time response, the cathode surface resistivity has been reduced by a factor 10, to reduce charge accumulations on the cathode when chamber operates at high rate, lowering from  $1\text{ M}\Omega/\square$  to  $100\text{-}200\text{k}\Omega/\square$  resistivity on the graphite layer. At the same time, cathode-readout plane (strips or pads) distance was reduced to 0.1mm(1.6mm before) to increase the capacitive coupling by 10, therefore the  $RC$  factor keeps unchanged.

The sTGC is made of two resistive cathodes planes, with copper readout plane with strips on one layer and the other one with pads, with  $8\text{x}12\text{cm}^2$  area used for fast pattern recognition of tracks to select strips for read out. This represents a big advantage compared to the TGC, which does not have this feature.

The cathodes are made of FR4 with 1.4mm of thickness, where  $17\mu\text{m}$  of copper is etched for strips (pads), pressed with a  $100\mu\text{m}$  of FR4 over it and then sprayed with graphite to provide superficial resistivity.

The anodes are golden tungsten wires of  $50\mu\text{m}$  diameter, distributed at 1.8mm of distance between each other and a gas gap of 2.8mm. To work with such geometry, several tests were made to find the proper gas mixture[6]. The most suitable mixture has been found to be 55% ( $\text{CO}_2$ ) and a quenching gas, a primary ingredient is 45% of n-pentane( $\text{n-C}_5\text{H}_{12}$ ), which allows the chamber to work in a limited proportional region[7](see Section

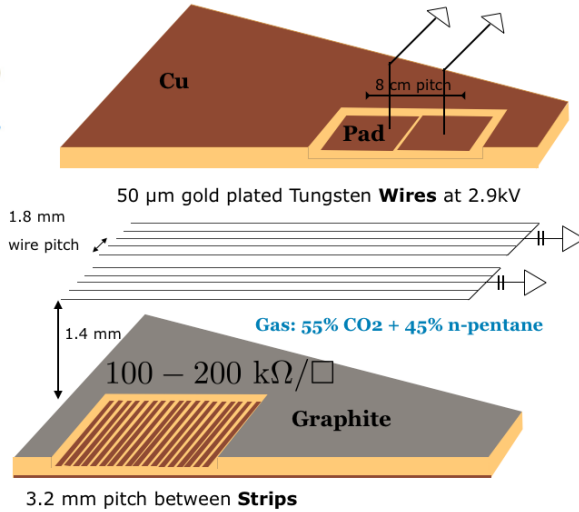


Figure 2.3: Single plane sTGC

1.2.3). The latest ingredient; n-pentane, can absorb UV photons due to its many molecular degree of freedom, hence preventing the chamber from going into a Geiger mode.

### 2.3.1. Electric field simulation

Motivated by gaining better understanding of the detector operational mechanisms, dedicated simulations studies using gaseous detector simulation tools have been performed. The main simulation tool used is Garfield [8, 9] software package. This set of libraries allows to calculate the electrical field with geometrical configuration as drift chambers.

The simulation uses a coordinate system where x is along the strips, y defines the chamber depth and z is along the wires.

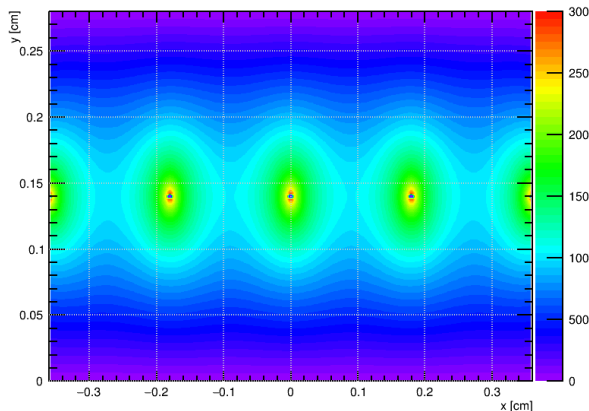


Figure 2.4: Equipotential lines, anode at 2900V

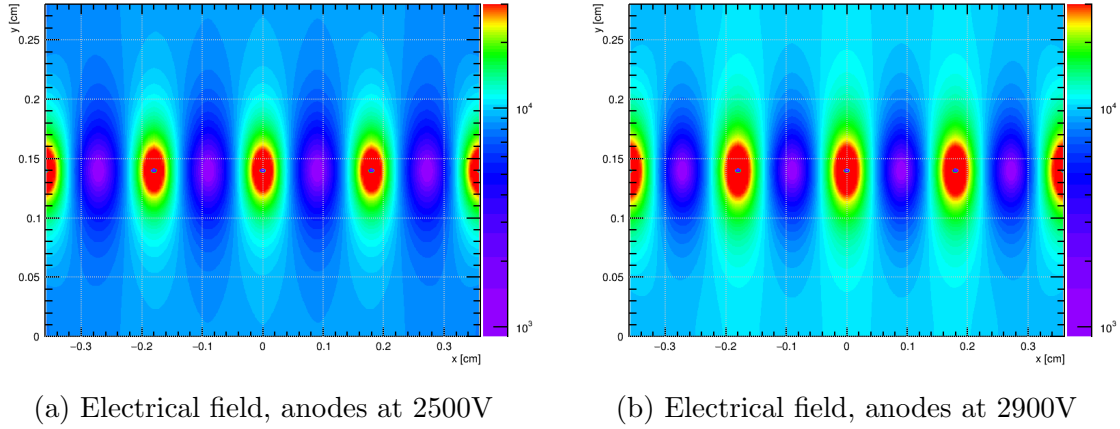


Figure 2.5: The electric field map in the x-y plane for a typical operating high voltage 2900V and 2500V.

Both contour plots on figure 2.5 represent the magnitude of the electrical field with scale of  $1 \times 10^3$  V/cm to  $1 \times 10^5$  V/cm with 50 steps. At the working potential 2.9 kV, it is possible to observed a field strength of more than  $1 \times 10^4$  V/cm over a 97% of the gas gap. The weakest field is only in a small region in the middle of two neighboring wires, leading to less than 5% of long drifting electrons.

## 2.4. Construction process

The main novelty on this detector is the high resolution obtained on x-axis due to the strip boards and the alignment between each chamber to get precision of about  $50\mu\text{m}$  and  $30\mu\text{m}$  respectively.

It is important to discuss the process which makes it possible to achieve these numbers. Everything relies on how well these chambers are built and also how the cathodes boards (strips and pads) are fabricated.

The size of each chamber varies from  $0.7\text{ m}^2$  to  $2.5\text{ m}^2$  with around 1m long, where over 300-400 strips must be etched with a precision of  $50\mu\text{m}$ . A standard length for printed circuit boards (PCB) is 70 cm. Extremely precautions must be taken to provide the precision and parallelism between each strips, in one of the biggest PCB board ever made.

The attempt of this section is to provide an overview of how the sTGC Quadruplets are built, mostly on the first module 0 produced by UTFSM, which is the QS1 (Quadruplet Small sector, part 1). Being the smallest detector to be produced for the NSW has some pros and cons. The main cons is related to the position of the QS1 inside the NSW; it is the closest one to the interaction point and as such, it gets the highest rate of particles. For the same reason, the position resolution is a key point and the high efficiency response under a high rate environment is a must.

Some pros are related to its size; with approximately 1.3 m long, 35 cm the small base

and 75cm the large one of the trapezoidal shape, the sTGC QS1 can be handled without any problems during its construction.

### Quality Control of cathode boards

The cathodes for the module 0 were made by an Italian company MDT, and since it was the first production, the review was done on-site.

The thickness of the board is measured in 19 points around the perimeter with a micrometer. The values of these measurements must be within  $1.5\text{mm}\pm25\mu\text{m}$ . Exceeding this numbers leads to the partial rejection of the cathode boards, however if there is a single point deviation of less than  $35\mu\text{m}$  from the average, it could be used in combination with another cathode board that does not have the same local deviation. The raw data is found in appendix ??.

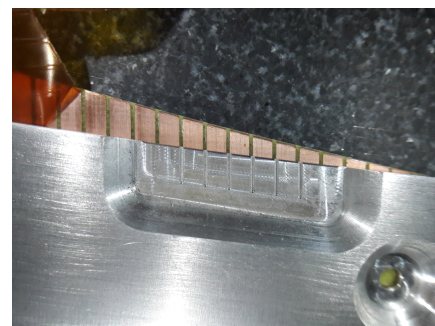
An electrical test is done with a multimeter, to check if there is any short circuit between strips or pads depending on the cathode board.

The last step and the most important is the dimensional control; it is performed on a granite table, with 2 pins that match the brass inserts on the cathode and a special caliper.

An aluminum-ruler (Al-ruler) machined (see Figure 2.6a) with a precision of  $30\mu\text{m}$  at 20 Celsius degrees is used as caliper. Above the cathode board the misalignment is measured. It has the same strip pitch for the first and the last five strips as well as two intermediate regions, and to avoid any parallax, the thickness of the edge for these strips is 1mm. Looking with a magnifying glass around 4 regions allows to detect some misalignment between these strips (caliper and cathode board). A photography is taken and analyzed to calculate this misalignment. For such distance (about 1 m long) some precautions must be taken, considering the expansion coefficient for both material.



(a) Al-ruler used to check shift over the last strips.



(b) Zoom-in Comparing strip position

Figure 2.6: Strip control with Al ruler

### Cathode preparation

Once the cathodes pass all the dimensional control, they have to be cleaned with Acetone and Isopropyl alcohol and placed on a granite table (with a flatness better than

$30\mu\text{m}$ ) with a vacuum system underneath. They have to be fixed on the edges with metal jigs which have marks for the internal wire support or chamber division.

The places which are not sprayed with graphite, like the wire support and the edges, are covered with a 3.5mm black tape on the designated wire support locations across the board. To prevent spraying graphite on the places where there will be glue, a blue tape must be placed on the edges.

### Graphite spraying

A key point for this process is to prepare the “painting”, a mixture of Graphite-33 with Plastik-70 bonding agent.

The graphite must be agitated for at least 2 hours before mixing with Plastik-70. A proper ratio of 1500g Graphite and 540g Plastik is mixed during 2 hours before spraying.

A spraying machine is in charge of this process, and meanwhile temperature and humidity must be controlled. After the cathode is painted, the superficial resistivity is measured on the edges. Values must exceed  $100\text{k}\Omega/\square$  otherwise the cathode needs to be sprayed again.

### Polishing

In order to ensure an homogeneous resistivity across the chamber, the cathode is visually divided in to  $5 \times 6$  sections. Inside each section, the resistivity is measured on 5 to 7 points with a probe. Simultaneously the cathode is brushed in the same orientation as the wires. The brush must be done carefully, without over-polishing areas, because once the resistance drops down, nothing will bring it back up.

### Gluing internal parts

After removing all the blue and black tapes, all the internal parts (buttons, wire support, etc.) are glued to provide mechanical support to the anode wires.

The wire support and the buttons help the chamber not to bend due to gravity and not to create a catenary effect. The external frames provide the 1.4mm height for the gas gap. All these part are cleaned with isopropyl alcohol, While the glue, a type of epoxy (2011-Araldite) is prepared, all these parts are cleaned with isopropyl alcohol. This glue will not only fix the parts, it will also fill the surfaces where these parts are less thick than requested.

### Winding wires

A flat table which can spin around one axis is used to wind the cathodes board. On each side of the table, one cathode with all the internal parts is tight with metal clamps on the edges. At the same time, vacuum is applied underneath to ensure the flatness of the cathode. A winding machine places each wire at 1.8mm distance from each other with  $50\mu\text{m}$  precision.

After the process is completed, all the wires are soldered in batches of 10 over the wire-rulers. The remaining wire can be cut and the HV resistors ( $10M\Omega$ ) soldered. The metal clamps around the edges are then removed, and the relative wire tension is checked by comparing the deflection of adjacent wires.

### Detector Assembly

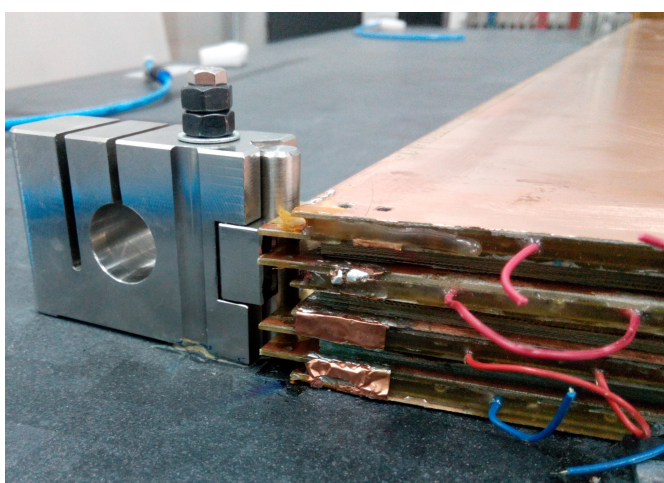
Once the cathodes are wound and all wires are soldered, the Pad cathode board is cleaned with clean water and dried with clean air. The board is placed on the granite table (with vacuum underneath) to be tested with high voltage. It is necessary to monitor the current from the cathode while the voltage is increased. It starts with 100V and reaches 3000V, with steps of 100V. The current should never reach a value higher than  $1\mu A$ . If it does, the cathode needs to be checked carefully, to remove dust or glue which create sparkles.

Reaching the nominal current, the strip cathode board is placed against the pad cathode board carefully. An aluminum frame with a silicon rubber is placed on top to isolate the chamber from the environment. Afterwards, vacuum is applied to this chamber and  $CO_2$  is flushing inside the chamber.

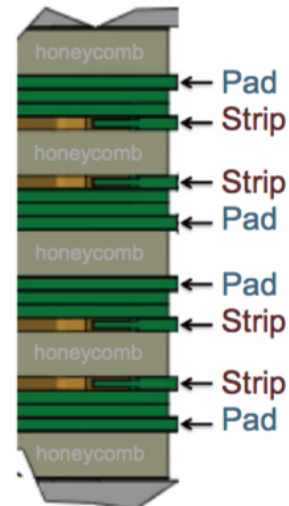
The power supply is turned on and no sparkles (monitoring the current) must be found.

In order to prevent dust entering the chamber, the glue is prepared to close it immediately. Upon completion of the process, a single chamber is built.

A doublet is assembled with two single chambers glued with a honeycomb paper. Repeating the process with two doublets, the quadruplet is built.



(a) Module #0 against alignment pin



(b) Layer description

Figure 2.7

## 2.5. Gain uniformity measurements

After the chambers are built, it is important to look for any malfunctioning. A primitive test to check the behavior of the detector is to move a radiation source across the sensitive area, while the current draw is measured from the power supply. **This test will give us the first answer of the gain of the detector.**

In this test, it is important to understand what can produce variation on the gain. There are two main factor that can produce gain variations on wire detectors. The first one is the “nature” gain fluctuations from the charge production in proportional counters which follow Polya distribution, however it is less pronounced in limited proportional mode such as sTGC working region.

The second one is related to the mechanical tolerances, this part has been very well known for 40 years as it is presented in Sauli’s book [10] about drift chambers from which we can conclude the following:

- Variations on the wire diameter of about 1% (fabrication precision) results in a 3% change on the gain.
- A  $100\mu\text{m}$  difference in the gas gap thickness (2.7mm) results in about 15% change on the gain.
- The effect of a wire displacement of about  $100\mu\text{m}$  of a wire plane results in 1% in the charge of the two adjacent wires which with a gain of  $\sim 10^6$  will give a  $\sim 10\%$  change on the gain.

Taking all of this in consideration, it is expected to get a gain variation of less than 20% in agreement with the Construction manual[11].

The amount of current measured from the power supply is considered as gain reference, while the detector is irradiated with x-rays. The test is performed under two different working points (bias voltage), 2500V (low gain) and 2900V, the operational voltage.

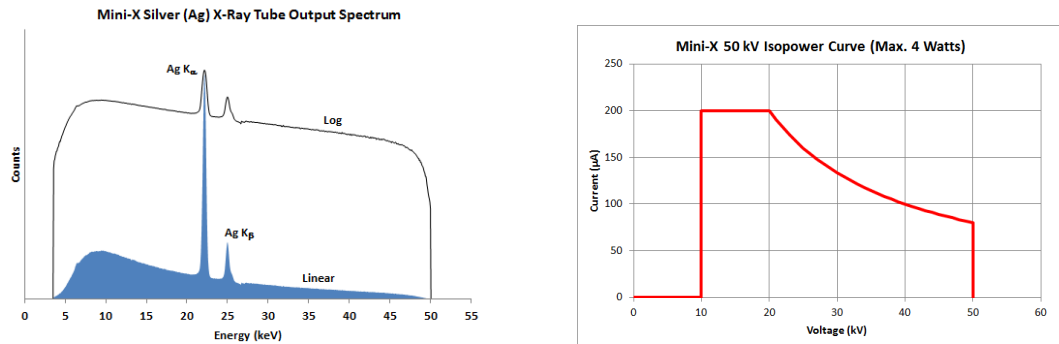
For such test the x-ray source is used due to the following advantages:

- Mostly mono-energetic photons.
- Variable photon intensity: Limiting the current from the tube from  $1\mu\text{A}$  to  $200\mu\text{A}$  can provide different rates.
- Variable photon energy: Varying the breaking voltage of electrons inside the x-ray gun from 10 kV to 50 kV.
- Different spot size: with a set of collimator it is possible to irradiate area of interest.

### 2.5.1. Setup

To perform such test, a x-ray gun called Mini-X[12] from Amptek is used, with silver (Ag) as transmission target and with a beryllium (Be) end-window.

The gun is mounted on a KUKA robo-arm (see Fig.2.9a), with a 5 degrees collimator providing a  $4\text{ mm}^2$  spot size at a proper distance. The robo-arm provides the x-y movement to scan the whole sensitive detector area, moving from the small base to the large base along the wires at step of  $1.2\text{ cm/s}$ (y – axis).



(a) Output spectrum, from 0 to 50keV

(b) Isopower curve for the Mini-x gun

Figure 2.8

(a) Mini-X gun mounted on KUKA  
robo-arm

(b) Collimator 2mm

Figure 2.9

The robo-arm moves along the x-axis in 5 cm/s steps. This is not the most suitable step to irradiate the whole detector, but it allows the x-ray gun to work properly at 45  $\mu$ A, 50keV energy (see figure 2.8b) without overheating.

A NIM HV Power Supply Module CAEN 1470 was used to power the chambers. The power supply (PS) was controlled by USB with the CAEN HV Wrapper Library. The current registered from the PS was written in a ASCII file for further analysis. The sampling rate used from the PS was 1 per second, giving the current average during this period. The test is taken in approximately one hour, irradiating one chamber at the time.

Since the detector is already built as a quadruplet, it has to turn over to irradiate its other face. Hence, only the external layers (chambers) are irradiated directly without having an chamber to provide a screening effect.

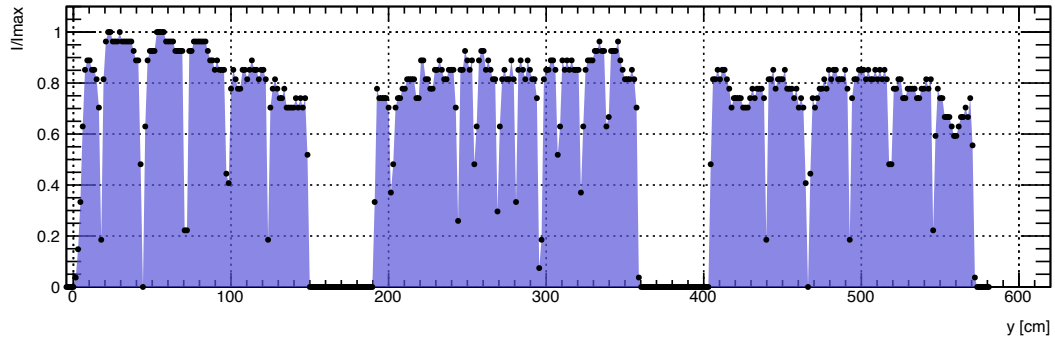


Figure 2.10: Relative current to the maximum, while the robo-arm is moved along the wires. The three set current corresponds to the whole detector irradiated in three different positions from x-axis.

### 2.5.2. Results

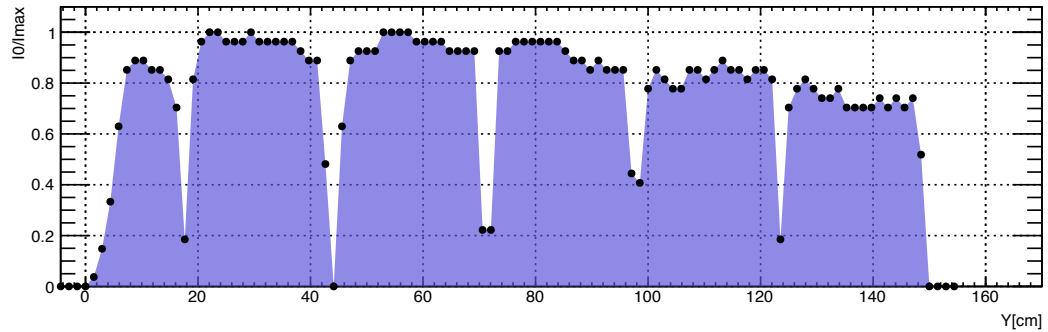


Figure 2.11: Moving across strips, wire-supports are present with minimum gain.

At first glance, it is possible to observed the internal structure of the chamber with this test. Looking at the Figure 2.11 the current decreases when the gun is irradiating

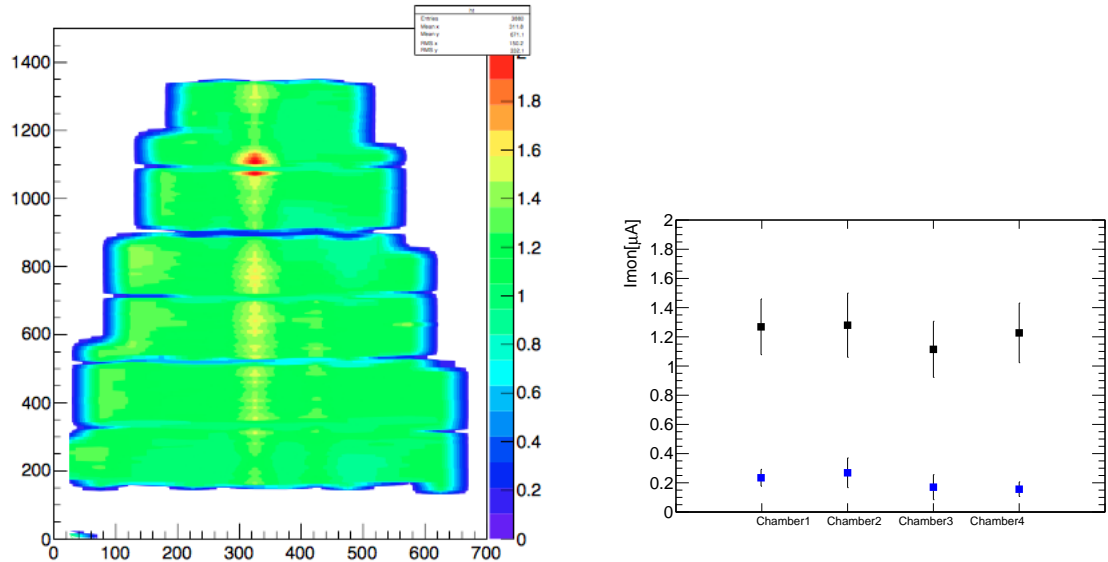
	Chamber 1	Chamber 2	Chamber 3	Chamber4
$\sigma/\text{mean}\%$	15.08%	17.18%	17.25%	16.64%

Table 2.2: Uniformity gain

the places where the wire-supports are found. In these places a small gas volume is present, therefore less electrons can drift to the wires, resulting in less current draw from the power supply.

If a better meshing of the irradiation places could be performed, identification of the wire-supports and the chamber separation (small and large sector) could be obtained with good resolution. For internal parts of 20mm, a width from 17 mm to 23 mm has been obtained with this test.

Interpolating the points  $(x, y, I)$ , an overall picture can be obtained (Figure 2.12a). The figure shows a line with high current resulting from a missing wire on the Chamber3. More charge is collected by the neighbors when a wire is missing, resulting from a longer drift path.



(a) xy-scan Chamber3 sTGC Module #0: (b) Current draw at 2.5kV (blue) and 2.9kV(black)

Figure 2.12

The graph on Figure 2.12b shows the average current from each Chamber at two different working potential. The average is calculated only for the sensitive area, hence, only values where the wire-support are not present form part of the average. The average current values at 2.5kV and 2.9kV are 200 nA and 1.2  $\mu\text{A}$  respectively.

The Table 2.4 summarizes the uniformity obtained, calculated as the RMS over the mean from the current draw distribution for each chamber. The four chambers have less

than 20% of gain variation, which was expected from the construction manual.

## 2.6. Stability under high rate

One of the key feature of this detector is that it must be able to work under high particles flow rates ( $15\text{kHz}/\text{cm}^2$ ), and the first step is to check whether the device or its electronic components can handle this high rate.

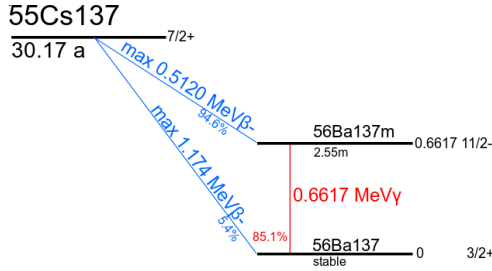


Figure 2.13: Cesium-137 Decay scheme.

For this purpose, the Module#0 was placed inside a new High Radiation Facility at CERN called GIF++[13]. The installation has a Cesium-137 (Figure 2.13) as a gamma source with an activity of approximately  $14.9\text{TBq}$  ( $13.3\text{TBq}$  during the test, August 2016). A system of movable lead attenuators (Figure 2.14a) for large irradiation zone allows attenuation factors between 1 and  $5 \times 10^5$  in several steps.

In order to get a reference of the particle rate, a direct measurement setup was implemented with a small size ( $16.2\text{ cm} \times 12.4\text{ cm}$  as sensitive area) sTGC as a **Monitor**. A LVDS (Low voltage differential signaling) logical signal from wires was obtained from an Amplifier Shaper Discriminator (ASD) board[14] connected to this Monitor. The ASD board provided the signal from 16 wires groups, all of them connected to a VME module (KEK ASD buffer), which controls the threshold from the discriminator on the ASD and converts the LVDS to NIM signal. The 16 LVDS signals are converted into two NIM logical signals. The two outputs from the module are connected to a Scaler NIM n145 which provides the number of positive NIM signals from the 16 channels in 10 seconds.

The Module#0 and the Monitor were placed at  $1.3\text{m}$  distance from the radioactive source. Both were connected in series to the same gas line ( $^{137}\text{Cs} : 45\text{n} - \text{C}_5\text{H}_{12}$ ), and the temperature and pressure were recorded to keep track of the working voltage. Most of the time, the environmental conditions were measured at 25 Celsius degree and  $971\text{mb}$ .

The working potential for the chamber is  $2850\text{V}$  at  $1\text{b}$ . Since the gain is proportional to  $E/P$ , where  $E$  is the electrical field and  $P$  the pressure inside the chamber, the voltages must be decreased by 2.9% to compensate the lower pressure, resulting in a  $2765\text{V}$  as the new working point in this environment.

To achieve the background rate for ATLAS ( $15\text{kHz}/\text{cm}^2$ ), the Monitor must register more than  $2680\text{ kHz}$  if the sensitive area is considered. The sensitive area is calculated as the total area  $200\text{ cm}^2$  times the amount of wires group connected to the ASD.

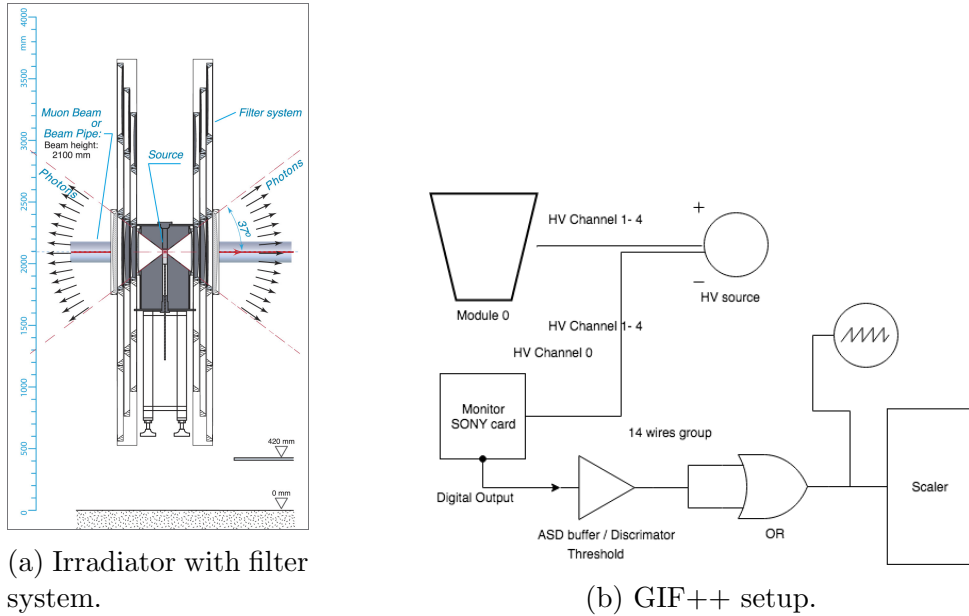


Figure 2.14: Three different rows with three lead (Pb) layers, each one with different thickness to provide multiples rates for the facility.

Four different attenuation factors were registered (10, 4.5, 2.2 and 1). On Figure 2.15a it is possible to observe two sets of data with rates over than the expected one (red and blue). The other two sets of data emphasize the *plateau* reached over 2.7kV. At the same time, the highest rate shows an inefficiency on voltages over 2.8 kV and the *plateau* is lost. Therefore, the data set with attenuation 2.2 (in red) is our reference.

Multiplying the attenuation factors with each data set (Figure 2.15b) should give us the expected rate with no filters. However, the data set with factor 1 has 5 MHz at working potential (2.9kV), while the expected rate from data sets attenuation 10 and attenuation 4.6 is 6.6 MHz. When comparing the rates from data set 1 with these, we observe an efficiency of about 75% of the expected rate. Then, comparing the data set 2.2 with the lowest rates results in approximately 93% of efficiency.

These findings may suggest a change in the gamma spectrum emitted after the attenuation filters. For a comprehensive analysis, a detailed study of the spectrum can be found in Chapter 3.

The flow rate recorded in data set 2.2 is 28 kHz/cm<sup>2</sup>, if we compensate the inefficiency the total flow rate is 30 kHz/cm<sup>2</sup>, which is the double than expected as a background level for ATLAS. Therefore the sTGC detectors must be tested against attenuation factor lower than 4.4.

Once the Monitor is set, the quadruplet is connected to the high voltage power supply. Each layer is internally divided in two sections, a small sector (S0) and large sector (S1). Each one of these sectors is powered independently on each channel from the CAEN High Voltage power supply A1833P (4 kV/2 mA max). The current from each layer (two sectors each one) was recorded with a resolution of 0.1  $\mu$ A. Four different attenuation filters were applied, and the results are shown in Figure 2.16.

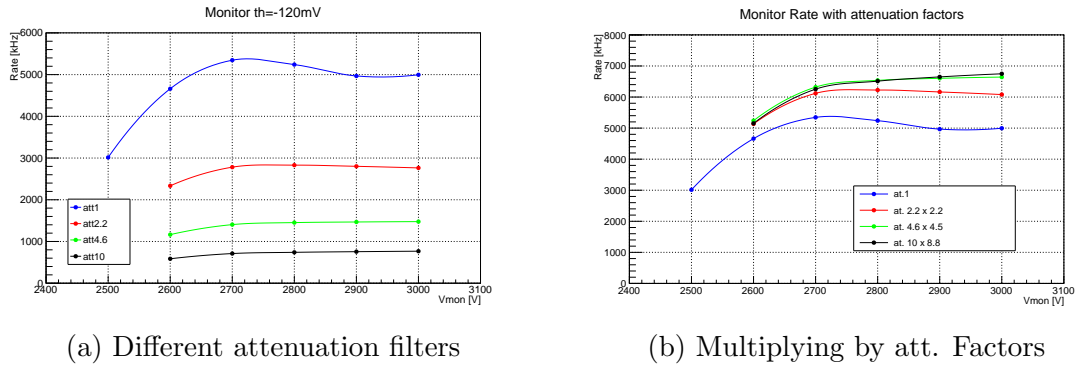


Figure 2.15: Rate on Monitor

$$\Delta\% = \left| 1 - \frac{I_1/I_0}{A_1/A_0} \right| * 100 \quad (2.1)$$

$A_1/A_0$	Layer 1		Layer 2		Layer 3		Layer 4	
	Filter	$I_1/I_0$	$\Delta\%$	$I_1/I_0$	$\Delta\%$	$I_1/I_0$	$\Delta\%$	$I_1/I_0$
10	2.49	1.58	3.02	8.63	3.01	1.95	3.08	9.41
4.6	2.34	7.51	2.87	3.24	2.73	11.07	2.87	15.59
2.2	2.29	9.49	2.79	0.35	2.68	12.70	2.67	21.47
1	2.22	12.25	3.02	8.63	2.45	20.19	2.49	26.76

Table 2.3: Comparison between sensitive area ratio ( $A_1/A_0$ ) from large and small sectors with the ratio of current ( $I_1/I_0$ ) at 2.9kV. A percentage difference column ( $\Delta\%$  defined in equation 2.1) is calculated to highlight the incremental disagreement as the gamma rate increases.

These results shows a linear dependency of voltage, with lower resistance as the rate of particles is increased. It is also important to notice that each wire group is connected to a  $10\text{ M}\Omega$  resistor, however not all the wires have the same length (the chamber has a trapezoidal shape), resulting in a lower voltage drop from the external groups where the wires are shorter (collecting less charge).

The Table 2.3 compares the area ratio between the internal sections of each chamber with the current registered for each set of measurements. The effect of dropping voltage appears to be the explanation of the incremental disagreement of the area ratio as the rate increases. The larger percentile difference is observed on the Layer 4 where the larger section is bigger than the previous ones, hence, the current ratio is lower.

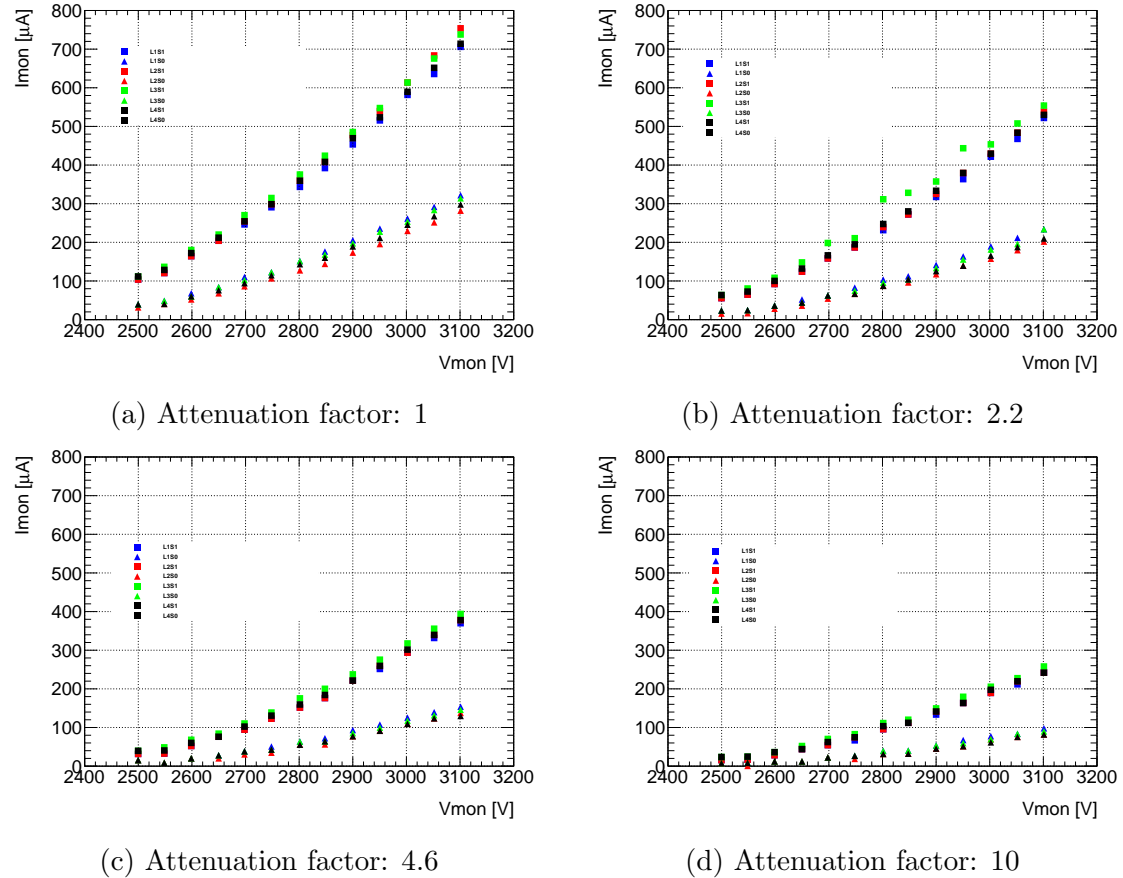


Figure 2.16: Current registered on the power supply for each chamber, large (S1) and small sector (S0) against applied voltage on anode.

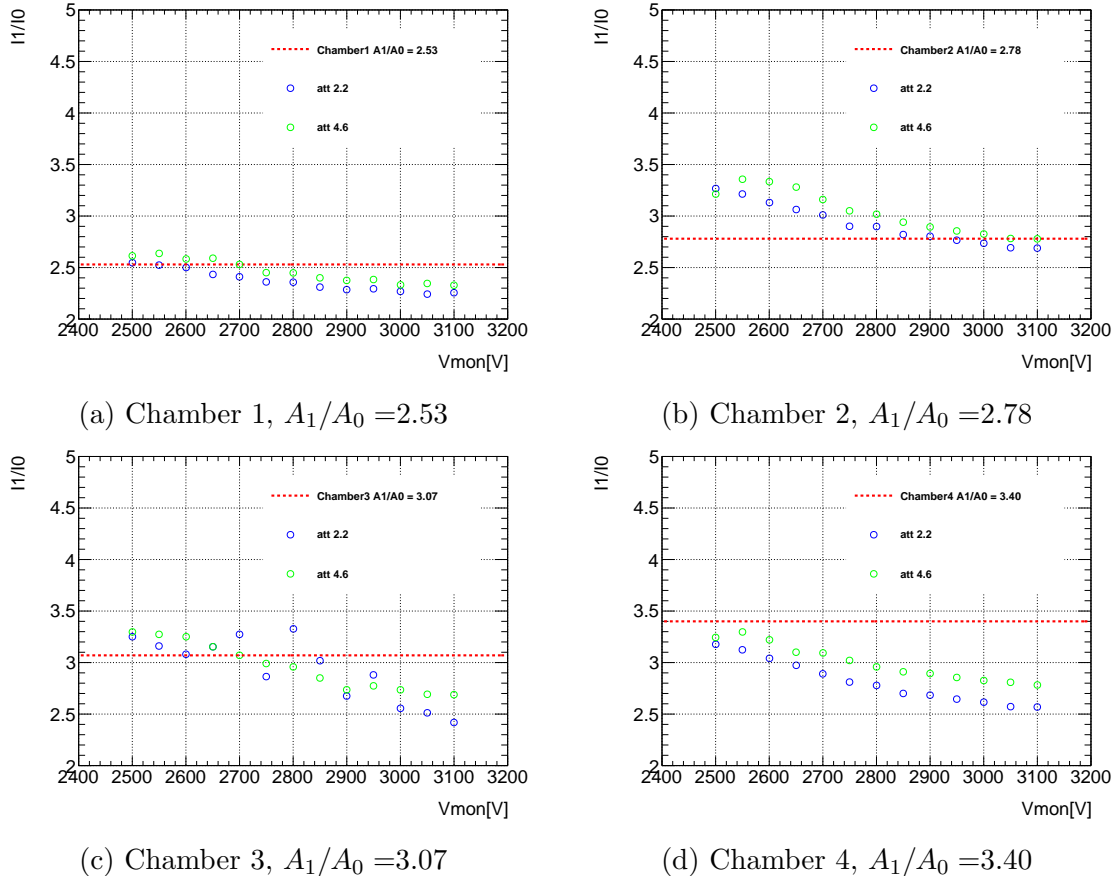


Figure 2.17: Current ratio  $I_1/I_0$  for two different rates compared with the area ratio  $A_1/A_0$  at different anode voltage. The Chamber 3 in (c) has a missing wire in the large section ( $A_1$ ), therefore the area ratio must be slightly lower and an increase of the current can be expected for the same reason.

## 2.7. Spatial Resolution

In order to achieve the precision reconstruction of tracks (offline) with a spatial resolution of about  $100\mu\text{m}$  per sTGC layer, and fast trigger on the region of interest (ROI) with Pads, two test beams were done.

In the spring of 2014, the Weizmann Institute of Science in Israel built the first full-size sTGC quadruplet detector of dimensions  $1.2 \times 1.0\text{m}^2$ . This prototype consists of four sTGC strips and pad layers and is constructed using the full specification of one of the quadruplets to be used in the NSW upgrade (the middle quadruplet of the small sector). The first test beam experiment took place at Fermilab with one goal in mind, to determine the position resolution of a full-size sTGC.

EUDET pixel telescope was used as a reference to measure the beam position, using the technology of 6 Minimum Ionizing MOS Active Pixel Sensor (Mimosa26) detectors with  $\approx 5\mu\text{m}$  position resolution. Three telescopes are placed in front of the beam, and three after the sTGC as is shown in Figure 2.18 with 15cm between them and 64cm between each arm. Each Mimosa26 detector has an active area of  $2.24\text{cm}^2$  made of CMOS pixel matrix of 576 rows and 1152 columns with  $18.4\mu\text{m}$  pitch.

A 32GeV pion beam was used at the rate of 1kHz over a spot of  $1\text{cm}^2$  giving to the sTGC a very precise pion trajectory thanks to the EUDET telescope. Event triggering was controlled by a custom Trigger Logic Unit (TLU). The TLU received signals from two  $1 \times 2\text{cm}^2$  scintillators placed in front and behind the telescope. The TLU generated the trigger signal that was distributed to the telescope and the sTGC readout electronics, which consists of a first application-specific integrated circuit (ASIC) called VMM1 which has the ability to read out both positive (strips, pads) and negative (wires) polarity signals, on 64 individual readout channels.

The VMM1 analog circuit features a charge amplifier stage followed by a shaper circuit and outputs the analog peak value (P) of the signal.

The readout of the ASIC is zero suppressed and thus only peak values of channels with signals above a predefined threshold are read. At the same time, the VMM1 may be programmed to provide the input signal amplitude of channels adjacent to a channel above threshold (neighbor-enable logic).

The precise position of a charged particle traversing an sTGC gas volume can be estimated from a Gaussian fit to the measured charge on adjacent readout strips (referred to as strip-clusters from here on). Given the strip pitch of 3.2mm and sTGC geometry, charges are typically induced on up to five adjacent strips.

The spatial sampling of the total ionization signal over a small number of readout channels means that a precise knowledge of each individual readout channel baseline is necessary in order to achieve the best possible measured spatial resolution.

The baseline of each individual readout channel was measured by making use of the neighbor-enabled logic of the VMM1 and its internal calibration system.

Test pulses were sent on one readout channel with the neighbor-enabled logic on, and baseline values were obtained by reading out the analog peak values of the two channels adjacent to the one receiving a test pulse.

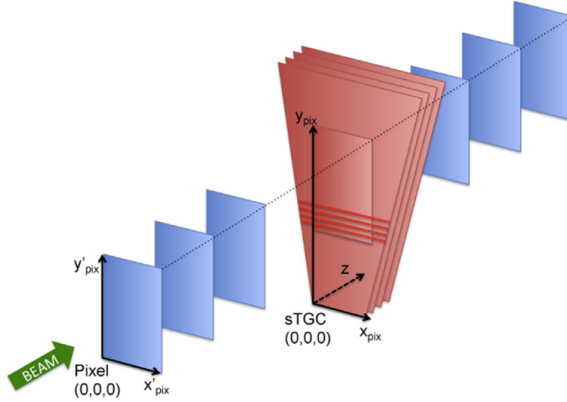


Figure 2.18: Schematic diagram of the experimental setup at Fermilab and coordinate systems used. Three layers of silicon pixel sensors are positioned before and after the sTGC detector. The dimensions are not to scale.

The silicon pixel hit positions were then used for reconstructing straight three dimensional charged-particle tracks. A track quality parameter was obtained for each fitted pion track based on the  $\chi^2$  of the track-fit. A small value of the track quality parameter corresponds to a straight track and a cut on this parameter can therefore be used to mitigate multiple scattering which are not considered in this analysis.

### 2.7.1. Analysis Model

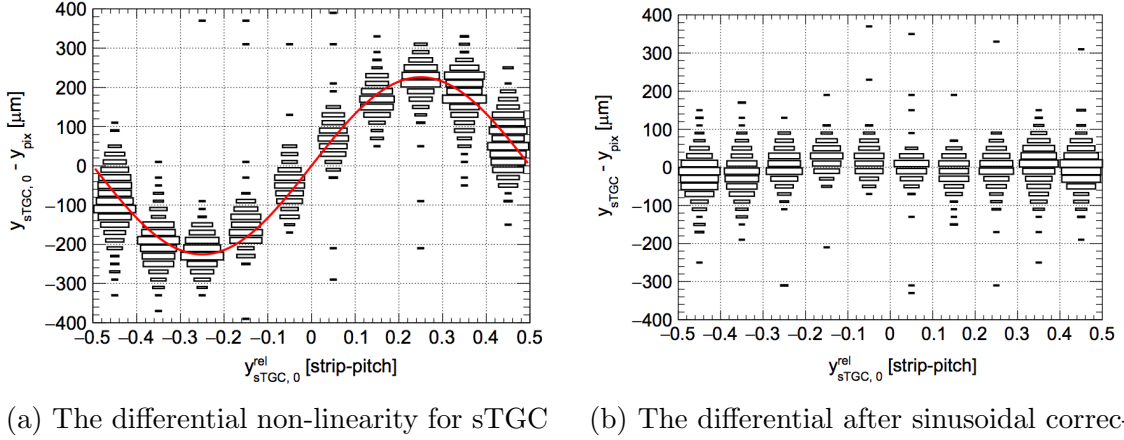
#### Pixel telescope analysis

In this model the intrinsic position resolution is obtained comparing the extrapolated beam trajectory from the pixel detectors with the measurements in each of the sTGC quad planes. Each layer is analyzed separately to reduce the effect of the multiple scattering and only tracks with  $\chi^2 < 10$  are considered for the same reason. From Figure 2.18 one can see that the  $y$ -axis is defined perpendicular to the strips, therefore sTGC strip-clusters provide measurements of the particle position in the  $y$ -direction( $y_{\text{sTGC}}$ ).

The position resolution is directly related to the profile of induced charge on the strips. The particle position is estimated from a Gaussian fit to the induced charge distribution on the strips. The neighbor-enabled logic of the VMM1 was used. Strip-clusters with induced charge in either 3, 4 or 5 adjacent strips are selected.

The pixel telescope tracks provide both coordinates,  $x_{\text{pix}}$  and  $y_{\text{pix}}$  at the position of the sTGC layer studied. The spatial resolution measurement is obtained by fitting the residual distribution  $y_{\text{sTGC}}$  and  $y_{\text{pix}}$  with a Gaussian model.

The charge measured on the strips of the sTGC detector results from a spatial sampling and discretization of the induced charge. The process of reconstructing the sTGC strip-cluster position from this sampling introduces a differential non-linearity effect on the reconstructed strip-cluster position.



(a) The differential non-linearity for sTGC strip-clusters      (b) The differential after sinusoidal correction is applied

Figure 2.19: Charge distribution over strip-pitch

Table 2.4: Fit parameters per cluster size

Strip-cluster multiplicity $i$	Amplitude parameter $a_i$
3	$205 \pm 9$
4	$206 \pm 4$
5	$211 \pm 5$

The deviation of the measured strip-cluster position from the expected position (estimated by the pixel telescope track) depends on the strip-cluster position relative to the strips. This dependence is clearly seen in the two dimensional distributions in Figure 2.19a. It shows the y-residual versus strip-cluster position relative to the closest inter-strip gap center  $y_{\text{sTGC},0}^{\text{rel}}$ . This effect is corrected using a sinusoidal function:

$$y_{\text{sTGC}} = y_{\text{sTGC},0} - a_i \sin(2\pi y_{\text{sTGC},0}^{\text{rel}}) \quad (2.2)$$

where  $y_{\text{sTGC},0}$  is the strip-cluster mean resulting from the Gaussian fit and  $y_{\text{sTGC}}$  is the corrected particle position estimator. The amplitude parameters are denoted  $a_i$  for the 3,4 and 5 strip-multiplicity (cluster size). These amplitude parameters are free parameters in the fit. The values of the amplitude parameters obtained from the fit to data are compatible with being equal for the three strip-cluster multiplicity as shown in Table 2.4.

The correction function is therefore universal and is shown in Figure 2.19a. The two dimensional distribution after the correction is applied was found to be reasonably flat as shown in Figure 2.19b.

The alignment of the coordinate system of the pixel telescope with respect to the above-defined coordinate system of the sTGC layer also affects the measured residual distribution. A simple two-parameter model is used to account for translations and rotations of the two coordinate systems with respect to each other. Both the alignment correction and the differential non-linearity correction are included *in situ* in the analysis.

The alignment correction is introduced in the model by expressing the pixel track

position in the sTGC-layer coordinate system  $y_{\text{pix}}$ , as a function of the track position in the pixel telescope coordinate system  $x'_{\text{pix}}$  and  $y'_{\text{pix}}$ , and two misalignment parameters  $\delta y$  and  $\phi_{xy}$ , as follows:

$$y_{\text{pix}} = -x'_{\text{pix}} \sin \phi_{xy} + y'_{\text{pix}} \cos \phi_{xy} + \delta y \quad (2.3)$$

The variable  $\delta y$  corresponds to a misalignment along the y-axis of the sTGC coordinate system, and  $\phi_{xy}$  corresponds to a rotation of the telescope coordinate system in the x-y plane around the z-axis of the sTGC coordinate system. Translation and rotation misalignment along and around the other axis are not taken into account in this model, since they are expected to have a small impact on the determination of the intrinsic position resolution.

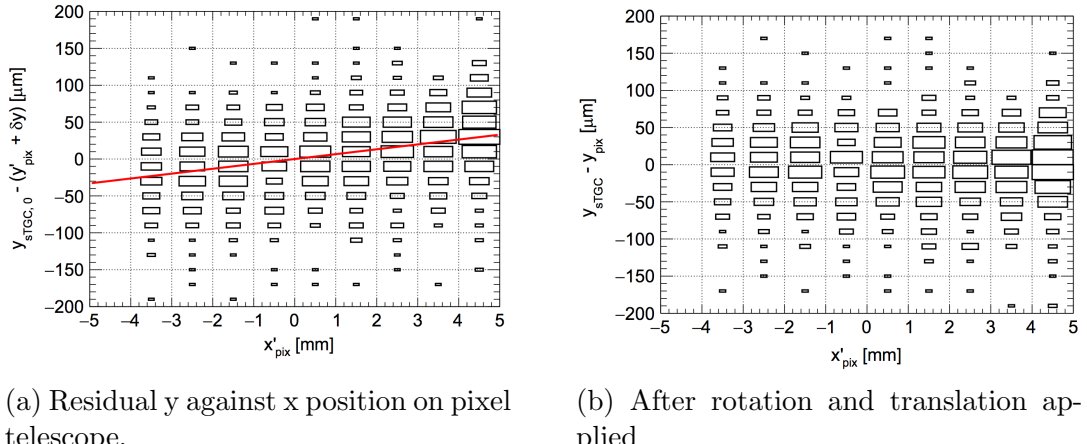


Figure 2.20: Coordinate system correction

On the Figure 2.20a it is possible to observe the y-residual mean increase linearly as a function of the x position on the telescope called  $x'_{\text{pix}}$ , which is evidence for a small rotation between the two coordinate systems. The red line represents the correction applied to this dataset. Accounting for this correction results in a distribution that is independent of  $x'_{\text{pix}}$  on Figure 2.20b.

After all the corrections are applied, the calculations for the intrinsic resolutions are taken for each layer and compared with the residual distribution. A double Gaussian function (equation 2.5) is fitted, where the first Gaussian represents the core of the residual distribution and the second one is a wider Gaussian which represents some reconstructed strip-cluster from background sources.

$$F_i = F_i(y_{\text{sTGC},0}, y_{\text{sTGC},0}^{\text{rel}}, x'_{\text{pix}}, y'_{\text{pix}}; \delta y, \phi_{xy}, a_i, \sigma, f, \sigma_w) \quad (2.4)$$

$$= fG(y_{\text{sTGC}} - y_{\text{pix}}; 0, \sigma) + (1 - f)G(y_{\text{sTGC}} - y_{\text{pix}}; 0, \sigma_w) \quad (2.5)$$

On Figure 2.21 a set of events shows the distribution presented before with an intrinsic resolution parameter  $\sigma$  of about  $44\mu\text{m}$  for a representative data taking run and sTGC

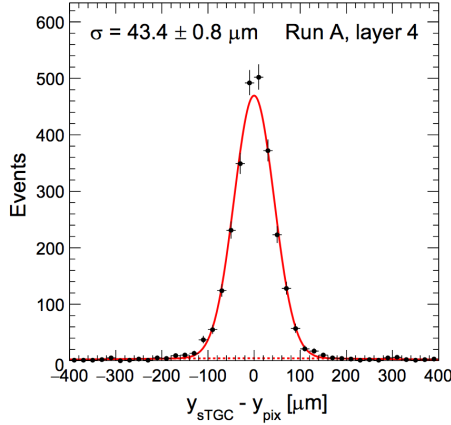


Figure 2.21: Intrinsic resolution of layer 4, respect to pixel telescope.

strip-layer, where the red line is the narrow Gaussian fit and the dashed line is the wider Gaussian fit.

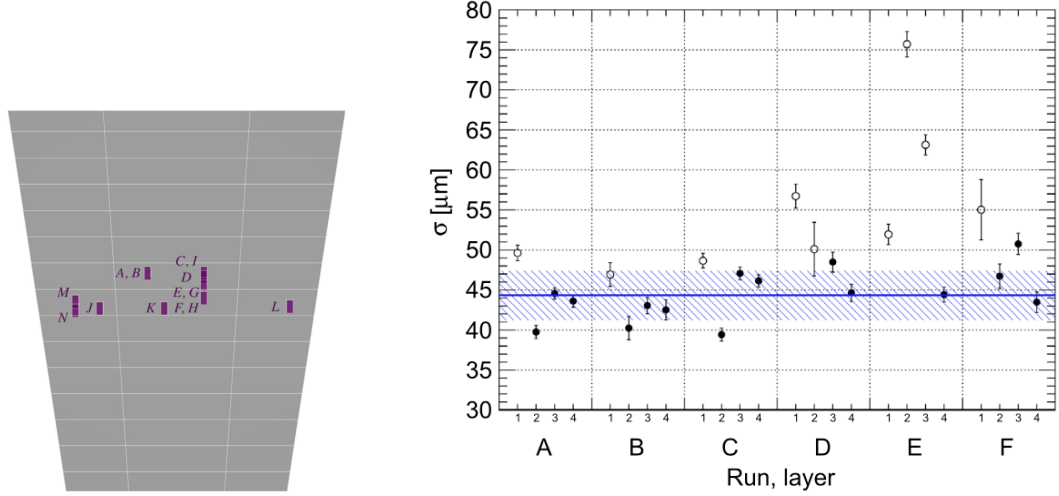
The fraction of the data parameterized by the narrow Gaussian is around 95% with a RMS of about 2%. The rest of data taking runs and its beam position can be observed on Figure 2.22b, where the black circles represent the valid data and the open circles the runs with expected degradation due to detector structure supports or individual channel pedestal.

### sTGC standalone analysis

In this analysis the correction for the differential non-linearity in respect to strip-pitch obtained before is kept, however the residual distribution of the y-position is calculated from two pairwise layer of the sTGC. Therefore half of the variance of this distribution corresponds to our parameter to estimate the intrinsic resolution for one layer, hence  $\sigma = \sigma_{\text{residual}}/\sqrt{2}$ .

A strip-layer position residual distribution for a representative sTGC standalone data taking run is shown in Figure 2.23a. In this graph, a intrinsic resolution of  $\sigma = 40.8 \pm 0.8 \mu m$  is obtained.

In summary of fourteen data sets, the intrinsic resolution with this analysis is about  $45 \mu m$ . The white open circles on the graph 2.23b correspond to non-validate data due to wire-support position or mis-calibrations. The hash band represents the RMS spread and the blue line is the average.



(a) Beam position for different data sets on sTGC

(b) Summary of intrinsic resolution for each data set and layer of sTGC

Figure 2.22: Summary of pixel telescope analysis

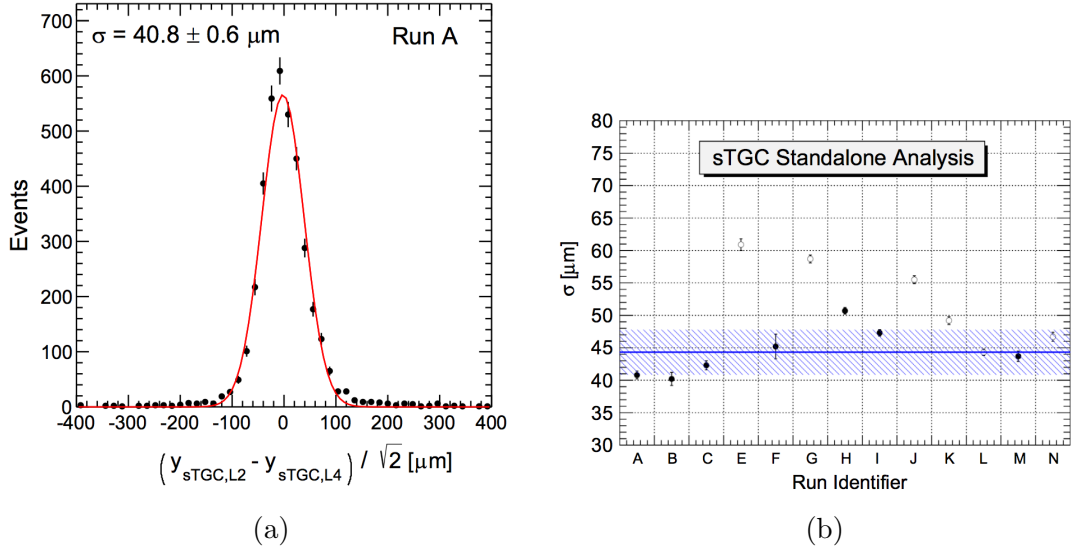


Figure 2.23: (a) Resolution estimate based on adjacent sTGC strip-layer position residual distributions for a representative sTGC standalone data taking run.

(b) Summary of the measured intrinsic sTGC resolution using the pixel telescope analysis for different data taking runs. The beam position on the sTGC detector for each run is shown in 2.22a. Results for runs with no expected degradation due to sTGC detector support structure or calibration are shown as black filled circles. The horizontal line represents the average resolution for these runs whereas the hashed band represents the RMS spread. Results for the remaining runs are shown as open circles.

## 2.8. Pad efficiency

One of the new features of the small-strip Thin Gap Chamber compare to its previous version is the possibility to provide a fast trigger for the Region of Interest from the  $8 \times 50 \text{ cm}^2$  pad area, where 3 out of 4 pads from a sTGC quadruplet can confirm a particle candidate, therefore a track position can be obtained from the strips within this area.

A test beam experiment was conducted at the CERN H6 beam line, using a 130 GeV muon beam of about 4 cm radius, a wider beam spot to test the characteristics of the pads. The setup is shown in Figure 2.24 where the system was triggered by a set of scintillators (in blue) with a  $12 \times 12 \text{ cm}^2$  coincidence area.

As explained before, for the beam tests a preliminary front-end electronics based on the VMM1 was used. This ASIC provides a Time-over-Threshold (ToT) signal as digital output, however is also possible to get a analog pulses. During the test beam, using the present configuration, an inefficiency was observed related to small late charges from the sTGC detector which may be not well adapted to the VMM1. An efficiency of 80-90% was observed running at  $100 \text{ kHz/cm}^2$ .

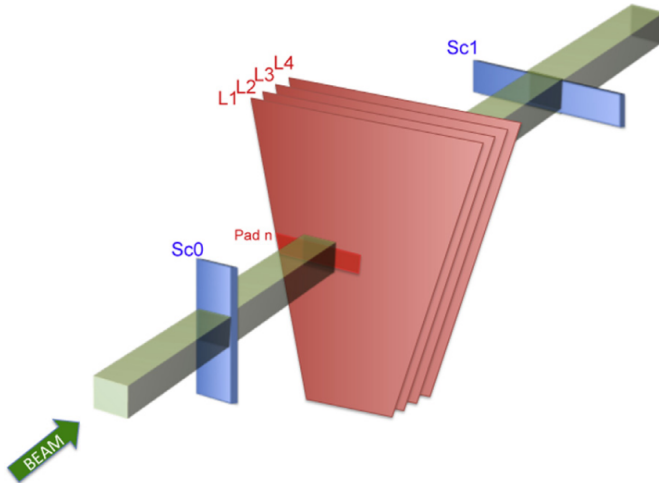


Figure 2.24: Setup for pad measurements. Coincidence block in light green. Pad  $n$  in red. Scintillators in blue.

To ensure that no inefficiency was due to the detector itself, the large cathode pads were used to estimate the detector efficiency, which was measured by looking at the analog output of the front-end amplifier. The efficiency of the pad  $n$  in the first layer was defined with respect to the coincidence of the trigger with a signal in the fully overlapping pad of the second layer.

Two examples from this configuration are shown on Figure 2.25; on the left a two analog signals from pads are present with a ToT signal from layer 1 with about  $2 \mu\text{s}$  length, meanwhile on the right picture a long ToT pulse with more than  $40 \mu\text{s}$  length when the two analog signal are present. By recording hundreds of triggered events using

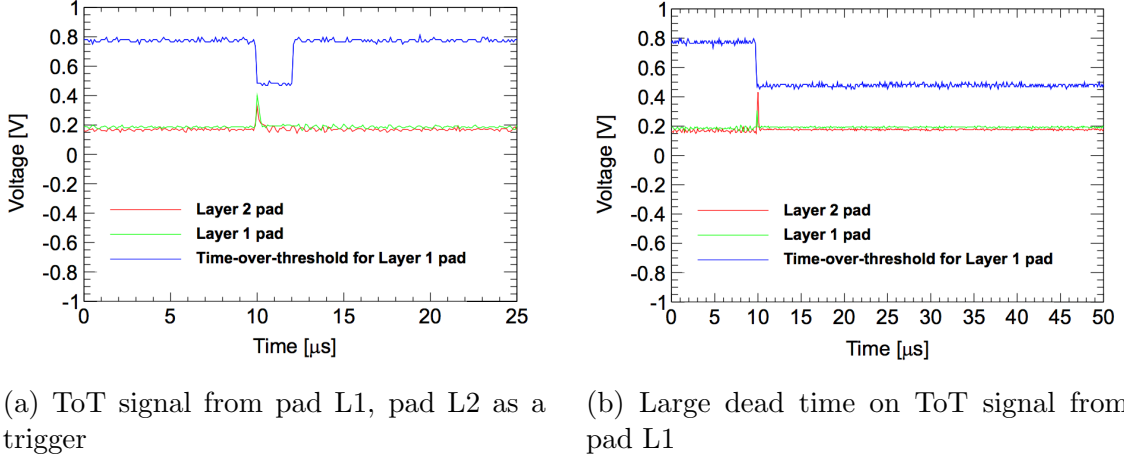


Figure 2.25: Digital and analog signal from VMM1

an oscilloscope, the presence of a detector signal within the live-part of the front-end electronics (independent of the signal threshold) was checked. This test confirmed that the detector was 100% efficient.

### Charge sharing between pads

To study the transition region between pads, the scintillator coincidence triggering area and the particle beam were centered between pad  $n$  and pad  $n + 1$  of the first layer, as illustrated in Figure 2.26a.

After applying timing quality requirements on the strip and pad hits, the channel baseline values are subtracted from the analog peak values. Strip-clusters with induced charge in either 3,4 or 5 adjacent strips are selected and calibrated in the same way as for the Fermilab beam test.

Events with a single strip-cluster in the first layer and the second layer are selected. The strip-cluster position (mean of the fitted Gaussian) in the first layer is used to define the position of the particle going through the detector. The events are further required to contain a hit above threshold on either pad  $n$  or pad  $n + 1$ . The charge fraction ( $F$ ) is defined using the analog peak values ( $P$ ) of the two adjacent pads:

$$F = \frac{P_n - P_{n+1}}{P_n + P_{n+1}} \quad (2.6)$$

Figure 2.26b shows the charge fraction as a function of the position with respect to the center of the transition region, where the two pads share more than 70% of the induced charge, spans about 4mm.

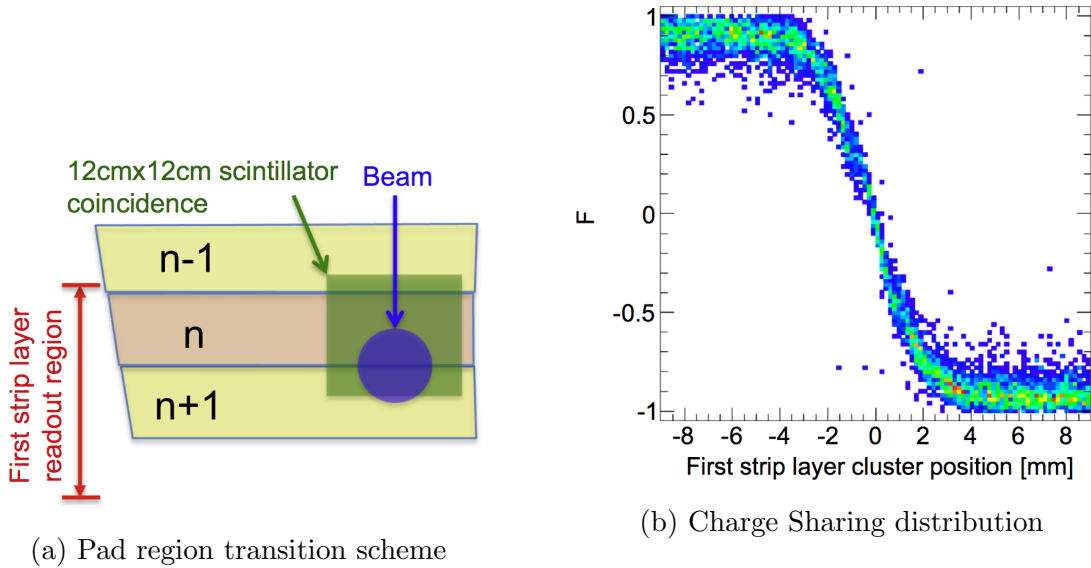


Figure 2.26

## 2.9. Summary

In the chapter we introduce the construction process and discuss the phenomenology of the sTGC. The main features of this Thin Gap Chamber are presented. The smaller strips of 3.2mm pitch give the spatial resolution needed for the improvement of the New Small Wheel of ATLAS. The main problem to achieve this precise  $3.2\text{mm} \pm 50\mu\text{m}$  pitch in long boards (1m to 2m long) is discussed.

To improve the time response the resistivity of the graphite layer is decreased and the distance between the readout and graphite layer is reduced to a  $100\mu\text{m}$ .

The sTGC detector is tested with four different objectives. The first test against x-rays occurs right after the Quadruplet is constructed. The use of this source helps to understand the construction issues as well as qualifying process, where the uniformity of the gain is measured.

Certainly, multiple factors can be improved in this test, such as increasing the vertical and horizontal steps to benefit from the 2mm spot size of the x-ray gun. Although the entire process for this test can be improved, the Module#0 shows an overall 17% uniformity for the four chambers.

In the Section 2.6 a direct measurement of the rate in a high irradiation environment is provided by a small size sTGC. The references values obtained help to set a working point to test the new Quadruplets against high flow rate. The non-linear change in the resistivity of the chamber for different particles rates suggests a better election for the resistor component connected to the anode wires. All the group wires are connected in series to a  $10\text{ M}\Omega$ , however, not all the groups receive the same amount of charge in an homogeneous particle rate because of the different lengths in the trapezoidal shape of the sTGC.

The last two sections summarize the two test beams for the first sTGC prototype, where crucial results are obtained for the electronics in charge of the readout. The test beam in CERN helps to understand the inefficiency of the Pads. The electronics designed for this detector (VMM1) has some issues which provides a 80-90% efficiency running at  $100 \text{ kHz/cm}^2$ . The detector is discarded, therefore, the VMM1 needs to be improved.

On the sTGC technology, all the efforts go to the improvement of the position resolution and the Section 2.7 shows a intrinsic resolution of about  $40 \mu\text{m}$  for the standalone analysis.

The spatial resolutions and pad efficiency results have been published in “Performance of a full-size small-strip thin gap chamber prototype for the ATLAS new small wheel muon upgrade” [15].



---

### 3. High count rate $\gamma$ -ray spectroscopy in GIF++



---

## 4. Synchrotron radiation detector for $e^-$ tagging



---

## 5. Conclusion



---

## A. Appendix

- A.1. Mechanical Measurements sTGC Module 0**
- A.2. PMT RT7525 Data Sheet**
- A.3. NA64 Experiment:Data structure**
- A.4. NA64 Experiemnt:DAQ system**



# Bibliography

- [1] ATLAS collaboration, “*Observation of a new particle in the search for the Standard Model Higgs boson with the ATLAS detector at the LHC*”, Physics Letters B **716** (2012) 1–29.
- [2] CMS collaboration, “*Observation of a new boson at a mass of 125 GeV with the CMS experiment at the LHC*”, Physics Letters B **716** (2012) 30–61.
- [3] G.Mikenberg et al., *Thin-gas gap chambers for hadronic calorimetry*, Nucl. Instr. and Meth. A **265** (1988) 223–227.
- [4] The LEP Collaboration, *Precision Electroweak Measurements on the Z Resonance*, Phys. Rep. **427** (2006) 257–454.
- [5] V.Smakhtin et al., *Thin Gap Chamber upgrade for SLHC: Position resolution in a test beam*, Nucl. Instr. and Meth. A **598** (2009) 196–200.
- [6] S.Majeski, *A Thin wire chamber operating in a high multiplication mode*, Nucl. Instr. and Meth A **217** (1983) 265–271.
- [7] W. Blum, *Particle Detection with Drift Chambers*. Springer, 2008.
- [8] Garfield++, *Project web page*, <http://garfieldpp.web.cern.ch/garfieldpp/>.
- [9] R. Veenhof, *GARFIELD, recent developments*, Nucl. Instr. and Meth. A **419** (1988) 726–730.
- [10] F.Sauli, *Principle of operation of multiwires proportional and drift chambers*. CERN, 1977.
- [11] *sTGC construction’s manual*, <https://edms.cern.ch/document/1399978/1>.
- [12] *Mini-X Gun Datasheet*, <http://www.amptek.com/pdf/minix.pdf>.
- [13] GIF++, *The new Gamma Irradiation Facility*, <https://espace.cern.ch/sba-workspace/gifpp/>.
- [14] O.Sasaki et al., *ASD IC for the thin gap chambers in the LHC ATLAS Experiment*, IEEE Transactions on Nuclear Science **46** (1999) 1861–1864.

- [15] A. Abusleme et al., *Performance of a full-size small-strip thin gap chamber prototype for the ATLAS new small wheel muon upgrade*, Nucl. Instr. and Meth. A **817** (2016) 85–92.
- [16] NA64 Experiment, *Search for dark sectors in missing energy events*, <https://na64.web.cern.ch>.
- [17] D. Banerjee et al. [NA64 Collaboration], *Search for Invisible Decays of Sub-GeV Dark Photons in Missing-Energy Events at CERN SPS*, Physical Review Letters **118** (2017) 011802.
- [18] A. Andreas et al., *Proposal for an Experiment to Search for Light Dark Matter at the SPS*, CERN-SPSC-2013-034 **SPSC-P-348** (2013) 011802, arXiv:1312.3309.
- [19] *SPS beam lines*, <http://cern.ch/sba>.
- [20] D. Banerjee, P. Crivelli and A. Rubbia, *Beam Purity for Light Dark Matter Search in Beam Dump Experiments*, Adv. High Energy Phys. **105730** (2015) .
- [21] R. Cryttenden, *Synchrotron radiation detector for tagging electrons*, Nucl. Instr. and Meth. A **276** (1989) 643–646.
- [22] S. Gobain, *BGO Bismuth Germanate*, <http://www.crystals.saint-gobain.com/products/bgo>.
- [23] S. Gobain, *Prelude 420 LYSO*, <http://www.crystals.saint-gobain.com/products/prelude-420-LYSO>.
- [24] O. Soto et al., *Characterization of novel Hamamatsu Multi Pixel Photon Counter (MPPC) arrays for the GlueX experiment*, Nucl. Instr. and Meth. A **739** (2014) 89–97.